



Rapid inversion of seismic damage to masonry infill walls based on diffusion models

Tianyang Zhang^a, Yujie Lu^b, Yijie Cai^a, Weizhi Xu^{a,*}, Shuguang Wang^a, Dongsheng Du^a, Qisong Miao^c

^a College of Civil Engineering Nanjing Tech University Nanjing China

^b School of Civil Engineering Southeast University Nanjing China

^c Beijing Institute of Architectural Design Beijing China

ARTICLE INFO

Keywords:

Data-driven
Machine learning
Diffusion
Masonry infill wall
Damage evolution

ABSTRACT

Masonry infill walls, which are weak links in current seismic designs, rely on numerical simulations to evaluate their seismic performance. As traditional macroscopic and microscopic finite element modelling (FEM) cannot simultaneously account for the damage evolution process and achieve sufficient computational efficiency for masonry infill walls, this study developed a damage inversion model (DIM) for infill walls based on diffusion models. The DIM can extract features from the macroscopic interstory deformation process of existing structures and use them as prompts to directly generate the damage factor distribution of masonry infill walls under the corresponding conditions. By varying the sampling steps and noise schedule in the DIM generation process, it was found that for the denoising diffusion probabilistic model (DDPM), the sampling steps should be set to over 500 to achieve a structural similarity (SSIM) of 0.87 compared with the microscopic FEM results. Conversely, the diffusion exponential integrator sampler (DEIS) can achieve a DDPM accuracy of 90.51% using only 1% of the DDPM sampling steps, balancing computational efficiency and predictive accuracy. Therefore, the DEIS has the potential to be developed into larger, more complex models for predicting the damage distribution of infill walls throughout the entire seismic process.

1. Introduction

Historical earthquake events have demonstrated that the failure of nonstructural components can lead to both building functionality and considerable economic losses [1–6]. Field investigations of earthquake sites have revealed that earthquakes cause particularly severe damage to historic and unreinforced masonry structures [7]. However, as critical components of building structures, damage to various nonstructural elements, such as masonry infill walls, has not been sufficiently addressed in current methods for the seismic damage assessment of buildings.

Globally, non-load-bearing masonry walls are the most widely used type of infill walls. In recent years, research on masonry infill walls has focused predominantly on the application of novel bricks and reinforcement materials [8–17]. Che et al. [8] investigated the strengthening effects of engineered cementitious composites (ECCs) on brick-masonry walls. The experimental results demonstrated that the ECC cladding significantly inhibited damage to the inner surfaces of brick walls. The strengthened brick walls transitioned

* Corresponding author.

E-mail address: xuwz@njtech.edu.cn (W. Xu).

<https://doi.org/10.1016/j.engfailanal.2025.109371>

Received 17 November 2024; Received in revised form 26 December 2024; Accepted 2 February 2025

Available online 3 February 2025

1350-6307/© 2025 Elsevier Ltd. All rights are reserved, including those for text and data mining, AI training, and similar technologies.

from the brittle failure mode to rocking or sliding failure modes. Jing et al. [9] conducted an experimental study on the shear performance of brick masonry walls reinforced with textile reinforced concrete (TRC). Compared with unreinforced brick walls, TRC-reinforced brick walls exhibited better integrity and ductility in their failure modes. Lee et al. [10] designed a high-performance fibre-reinforced cementitious composite (HPFRCC) for the reinforcement of masonry walls and evaluated its failure mode and ductility. The study indicated that the failure mode of the HPFRCC-reinforced masonry walls exhibited ductile behaviour with a significant improvement in tensile strength.

In addition to research on new masonry wall materials, studies on the connection forms [18–20] between infill walls and frames, as well as seismic damage to masonry infill walls [21–25], have also garnered significant attention. Bhat et al. [22] utilised a digital image correlation (DIC) system to study the failure modes and complex interactions between infill walls and surrounding frames in detail. It was demonstrated that the masonry infill altered the deformation pattern of the RC frame by constraining the deformation of the columns, resulting in extensive flexural cracking along the entire length of the columns. Xie et al. [25] investigated the impact of pre-existing in-plane damage on the out-of-plane behaviour of masonry infill walls by conducting sequential in-plane and out-of-plane quasi-static loading tests on a series of masonry infilled concrete frame specimens. The experimental results indicated that neglecting the coupling interaction between the in-plane and out-of-plane forces could lead to a significant underestimation of the seismic damage to the masonry infill walls. Penava et al. [26] conducted static pushover tests on 1/2.5 scaled single-bay reinforced concrete frames with masonry infill walls to examine the impact of openings of various types, sizes, and positions on the shear resistance of the structure under different load combinations. Through extensive micromodel finite element simulations, shear resistance calculation formulas were developed for the structure, considering the load direction and the ratio of the opening area to the wall area [27].

Building on the aforementioned experimental studies, numerous damage assessment studies on masonry infill walls have been conducted using finite element simulation methods. Generally, these studies can be categorised into macroscopic [28–31] and microscopic [32–35] finite-element simulations. The advantage of macroscopic simulation methods lies in their clear physical significance, which allows the prediction of the in-plane mechanical behaviour of infill walls. These methods are convenient for use in large-scale assessments, such as evaluating the seismic performance of entire building structures, and they offer high computational efficiency. However, they have limitations in observing and evaluating the detailed damage development process of infill walls. In contrast, microscopic finite-element simulations, although capable of providing a detailed analysis, currently have significant limitations. They often only refine the model to the scale of individual elements without further considering the bonding and interaction between the blocks and between the blocks and mortar [36]. These shortcomings are primarily due to the excessive computational demands of microscale simulations, which make them impractical for more detailed analyses [37].

The development of artificial intelligence (AI) technologies [38], particularly generative AI, offers new approaches for resolving the conflict between computational efficiency and accuracy in finite element simulations. For the first time, this study proposes an earthquake damage inversion method for infill walls based on cutting-edge diffusion models.

2. The problem of damage state identification of masonry infill walls during earthquakes

Earthquake damage assessments have revealed that nonstructural components, particularly infill and partition walls, frequently sustain significant damage. During design-based earthquakes, although the primary structural elements of a building may remain intact or exhibit only minor damage, masonry infill walls, particularly those constructed with block materials, often experience severe degradation [31]. This deterioration compromises the functionality of the building and can potentially lead to casualties and obstruct rescue operations following earthquakes. During the seismic design phase of building structures, numerous elastic–plastic time-history analyses are required to determine the seismic capacity of the structure. The increasing maturity of the finite element modelling (FEM) method has facilitated the calculation of earthquake collapse risk for structures. Typically, verification of the seismic capacity of an overall structure relies on the finite element method based on macro beam-column elements. Masonry infill walls are simplified as shell elements or equivalent diagonal strut models to consider the mechanical properties of infill walls, as shown in Fig. 1(a).

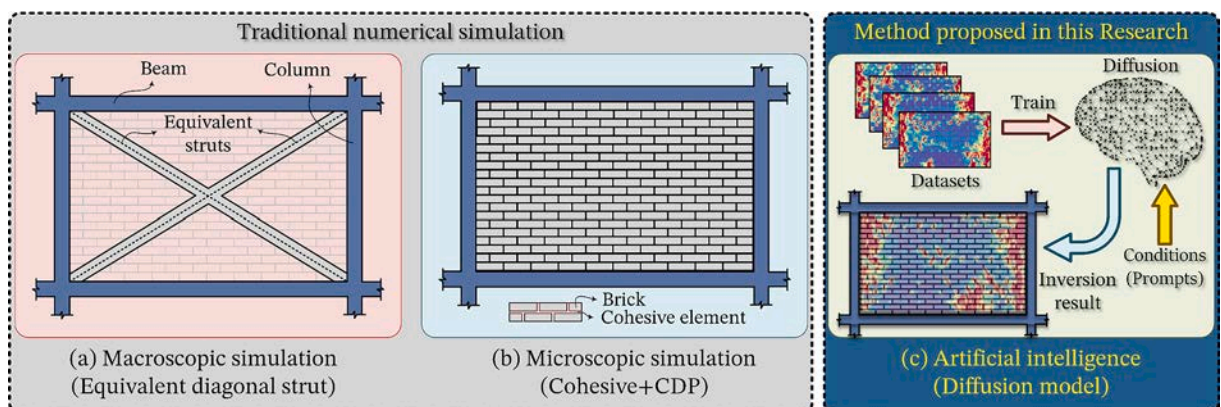


Fig. 1. Seismic damage calculation method of masonry infill walls.

Although macroscopic modelling approaches can achieve good computational efficiency, the accuracy of such methods is relatively low when applied to the overall behaviour of masonry infill walls owing to the inherent heterogeneity of the mortar and blocks. This limitation is detrimental to the assessment of earthquake-induced damage in infill walls. Microscopic numerical simulations using a separation-based FEM method, which assigns bonded slip properties to the cohesive elements surrounding the masonry elements to replace the function of the mortar, can yield more reliable simulation results [35]. However, owing to the complexity of the modelling process, its time-consuming nature, and substantial computational demands, conducting microscopic finite element simulations and assessing the seismic performance of the infill walls of the entire structure are generally deemed impractical, as shown in Fig. 1(b). Therefore, there is an urgent need to develop more accurate and rapid methods for calculating and assessing the damage states of masonry infill walls. As displacement-sensitive nonstructural components, damage to infill walls is solely associated with the interstory deformation of the structure. Establishing a mapping relationship between the damage state of infill walls and structural deformation can be used to facilitate the seismic performance evaluation of infill walls in regional buildings. With the advancement in AI technologies, it has become feasible to predict the damage state of masonry infill walls in response to displacement changes, as shown in Fig. 1(c).

3. Overview of the diffusion models

3.1. Diffusion model concept

Diffusion models [39] are a type of probabilistic generative model. The principle of diffusion models is to gradually add noise to the input data, thereby disrupting the original data distribution. Deep learning methods are then used for reverse denoising, thereby learning the distribution of the original input data. Diffusion models overcome the shortcomings of traditional generative adversarial networks (GANs), which only require training of the generator, without the need to train a discriminator [40]. The construction of the loss function is concise and auxiliary networks are not required. Therefore, this study adopts diffusion models as an inversion method for determining the seismic response of masonry infill walls.

The diffusion process originates from nonequilibrium thermodynamics. Nonequilibrium thermodynamics is dedicated to the study of physical systems that are not in thermodynamic equilibrium, such as the process of a drop of blue dye diffusing into water, as shown in Fig. 2. Before diffusion begins, the dye gathers into a darker spot in the beaker, and the probability distribution of the dye in water is difficult to describe at this point. As diffusion progresses, the dye gradually fills the entire beaker until the entire cup of water turns blue, at which point the system enters a state of equilibrium. After the diffusion is complete, the dye in the water is in a state of uniform distribution, and its probability distribution is relatively clear. A diffusion model based on nonequilibrium thermodynamics can establish the probability distribution of the dye at each time step as time progresses. If this process is reversible, a more complex distribution could be sampled from a simple distribution, thereby inferring the distribution of the dye in water at each moment.

3.2. Forward process

The denoising diffusion probabilistic model (DDPM) can derive more complex distributions from simpler ones [41]. The DDPM defines forward and reverse Markov chains. In the forward chain, Gaussian noise is gradually added to the input data. Subsequently, the diffusion process is learned in reverse, thereby converting the noise into the required data in the reverse chain, as shown in Fig. 2. The forward chain of the DDPM is redesigned to disrupt the distribution of the input features and gradually transform it into a prior distribution, typically a standard Gaussian distribution. If the original input feature x_0 follows the distribution $q(x_0)$, the forward chain generates a series of features x_1, x_2, \dots, x_T disturbed by noise through the transition kernel $q(x_t|x_{t-1})$. The transition kernel of a forward chain is defined as

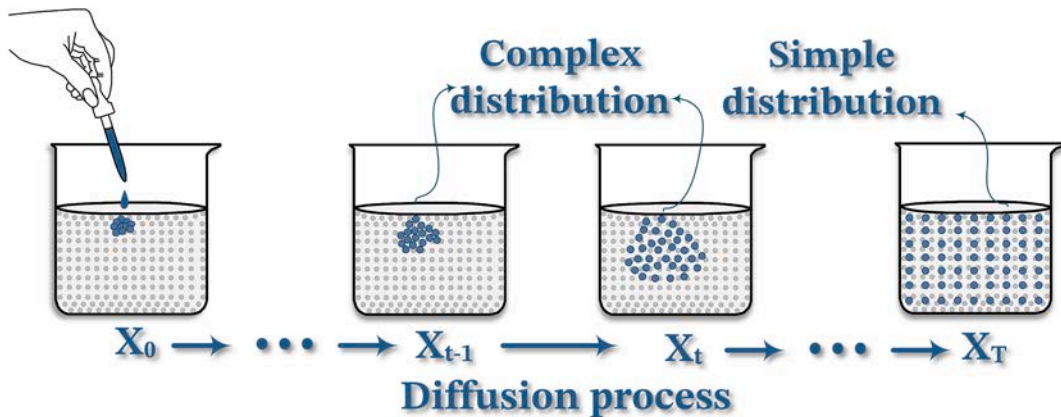


Fig. 2. Diffusion of dye in water.

$$q(\mathbf{x}_t|\mathbf{x}_{t-1}) = \mathcal{N}(\mathbf{x}_t, \sqrt{1-\beta_t}\mathbf{x}_{t-1}, \beta_t I) \quad (1)$$

and $\{\beta_t \in (0, 1)\}_{t=1}^T$. In DDPM, β_t is a predetermined hyperparameter that determines the intensity of the noise added at each step. Therefore, \mathbf{x}_t is a scaling of \mathbf{x}_{t-1} by a factor of $\sqrt{1-\beta_t}$, and noise with a variance of β_t is then added. Because the forward noise addition process in the DDPM is a Markov chain process, the result of each step depends only on the output features of the previous step. Therefore, the distribution of each step can be decomposed as follows.

$$q(\mathbf{x}_{1:T}|\mathbf{x}_0) = \prod_{t=1}^T q(\mathbf{x}_t|\mathbf{x}_{t-1}) \quad (2)$$

Here, \mathbf{x}_t can be obtained by reparameterizing Eq. (1) by Gaussian sampling.

$$\begin{aligned} \mathbf{x}_t &= \sqrt{1-\beta_t}\mathbf{x}_{t-1} + \sqrt{\beta_t}\epsilon \\ &= \sqrt{\alpha_t}\mathbf{x}_{t-1} + \sqrt{1-\alpha_t}\epsilon \\ &= \sqrt{\alpha_t\alpha_{t-1}}\mathbf{x}_{t-2} + \sqrt{1-\alpha_t\alpha_{t-1}}\epsilon \\ &= \sqrt{\alpha_t\alpha_{t-1}\alpha_{t-2}\cdots\alpha_0}\mathbf{x}_0 + \sqrt{1-\alpha_t\alpha_{t-1}\alpha_{t-2}\cdots\alpha_0}\epsilon \\ &= \sqrt{\alpha_t}\mathbf{x}_0 + \sqrt{1-\alpha_t}\epsilon \end{aligned} \quad (3)$$

where $\epsilon \sim \mathcal{N}(0, I)$, $\alpha_t = 1 - \beta_t$ and $\bar{\alpha}_t = \prod_{s=1}^t \alpha_s$. In the forward diffusion process, a relationship can be established between \mathbf{x}_t and \mathbf{x}_0 that satisfies the following distribution:

$$q(\mathbf{x}_t|\mathbf{x}_0) = \mathcal{N}(\mathbf{x}_t, \sqrt{\bar{\alpha}_t}\mathbf{x}_0, (1 - \bar{\alpha}_t)I) \quad (4)$$

As the number of diffusion steps increases, \mathbf{x}_T approaches the standard Gaussian distribution, and $q(\mathbf{x}_T) = \int q(\mathbf{x}_t|\mathbf{x}_0)q(\mathbf{x}_0)d\mathbf{x}_0 = \mathcal{N}(0, I)$.

3.3. Backward process

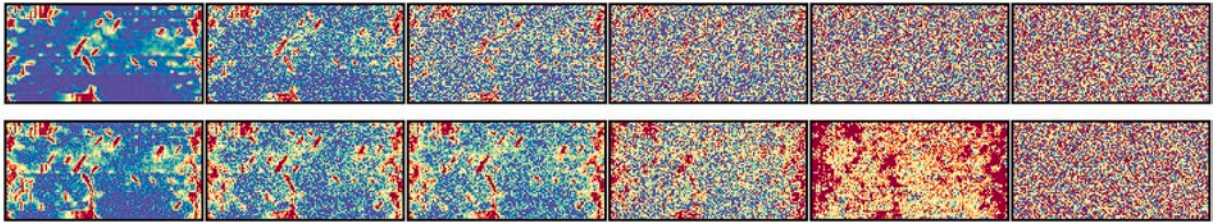
In the backward process, the DDPM initially generates unstructured noise, and then runs a reverse learnable Markov chain to gradually remove the noise and continuously generate new samples, as shown in Fig. 3. The purpose of the learnable transition kernel in the backward process is to denoise the normal distribution, thereby obtaining new features. This is defined as follows:

$$p_\theta(\mathbf{x}_{t-1}|\mathbf{x}_t) = \mathcal{N}(\mathbf{x}_{t-1}, \mu_\theta(\mathbf{x}_t, t), \Sigma_\theta(\mathbf{x}_t, t)) \quad (5)$$

$$p_\theta(\mathbf{x}_{0:T}) = p_\theta(\mathbf{x}_T) \prod_{t=1}^T p_\theta(\mathbf{x}_{t-1}|\mathbf{x}_t) \quad (6)$$

Given known $q(\mathbf{x}_{t-1}|\mathbf{x}_0)$ and $q(\mathbf{x}_t|\mathbf{x}_0)$ systems, the following probability relationship can be established based on Bayes' theorem:

Damage factor \longrightarrow Destructing data by adding noise \longrightarrow Noise



Damage factor \longleftarrow Generating samples by denoising \longleftarrow Noise

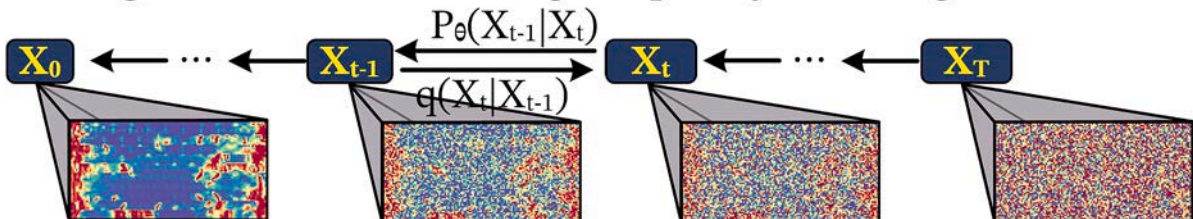


Fig. 3. Diffusion and prediction process of the DDPM.

$$q(x_{t-1}|x_t, x_0) = \frac{q(x_t|x_{t-1}, x_0)q(x_{t-1}|x_0)}{q(x_t|x_0)} \quad (7)$$

where the three variables in Eq. (7) satisfy the following relationship:

$$q(x_t|x_{t-1}, x_0) = \mathcal{N}(x_t, \sqrt{\alpha_t}x_{t-1}, (1 - \alpha_t)I) = \frac{1}{\sqrt{2\pi(1 - \alpha_t)}} \exp \left[-\frac{(x_t - \sqrt{\alpha_t}x_{t-1})^2}{2(1 - \alpha_t)} \right] \quad (8)$$

$$q(x_{t-1}|x_0) = \mathcal{N}(x_{t-1}, \sqrt{\bar{\alpha}_{t-1}}x_0, (1 - \bar{\alpha}_{t-1})I) = \frac{1}{\sqrt{2\pi(1 - \bar{\alpha}_{t-1})}} \exp \left[-\frac{(x_{t-1} - \sqrt{\bar{\alpha}_{t-1}}x_0)^2}{2(1 - \bar{\alpha}_{t-1})} \right] \quad (9)$$

$$q(x_t|x_0) = \mathcal{N}(x_t, \sqrt{\bar{\alpha}_t}x_0, (1 - \bar{\alpha}_t)I) = \frac{1}{\sqrt{2\pi(1 - \bar{\alpha}_t)}} \exp \left[-\frac{(x_t - \sqrt{\bar{\alpha}_t}x_0)^2}{2(1 - \bar{\alpha}_t)} \right] \quad (10)$$

Based on Eq. (8) to Eq. (10), it can be deduced that $q(x_{t-1}|x_t, x_0)$ follows the relationship below:

$$\begin{aligned} q(x_{t-1}|x_t, x_0) &\propto \exp \left\{ -\frac{1}{2} \left[\frac{(x_t - \sqrt{\alpha_t}x_{t-1})^2}{1 - \alpha_t} + \frac{(x_{t-1} - \sqrt{\bar{\alpha}_{t-1}}x_0)^2}{1 - \bar{\alpha}_{t-1}} - \frac{(x_t - \sqrt{\bar{\alpha}_t}x_0)^2}{1 - \bar{\alpha}_t} \right] \right\} \\ &= \exp \left\{ -\frac{1}{2} \left[\left(\frac{\alpha_t}{\beta_t} + \frac{1}{1 - \bar{\alpha}_{t-1}} \right) x_{t-1}^2 - 2 \left(\frac{\sqrt{\alpha_t}}{\beta_t} x_t + \frac{\sqrt{\bar{\alpha}_{t-1}}}{1 - \bar{\alpha}_{t-1}} x_0 \right) x_{t-1} + C(x_t, x_0) \right] \right\} \\ &\propto \mathcal{N} \left(x_{t-1}, \frac{\sqrt{\alpha_t}(1 - \bar{\alpha}_{t-1})x_t + \sqrt{\bar{\alpha}_{t-1}}(1 - \bar{\alpha}_t)x_0}{1 - \bar{\alpha}_t}, \frac{(1 - \alpha_t)(1 - \bar{\alpha}_{t-1})}{1 - \bar{\alpha}_t} I \right) \end{aligned} \quad (11)$$

By substituting Eq. (3) into Eq. (11), we can obtain $\mu_\theta(x_t, t)$:

$$\mu_\theta(x_t, t) = \frac{1}{\sqrt{\alpha_t}} \left(x_t - \frac{\beta_t}{\sqrt{1 - \bar{\alpha}_t}} \varepsilon_\theta(x_t, t) \right) \quad (12)$$

Here, ε_θ is a learnable parameter. With this Markov chain based on neural networks, we can sample the noise, iterate using the transition kernel, and finally generate x_0 .

4. Numerical simulation and dataset development

To perform seismic damage inversion and predict the damage process masonry infill walls, a large dataset for training must be established. However, obtaining such a large-scale and high-quality dataset of the infill wall damage from experiments is challenging. Therefore, this study employed experimental validation of the fundamental mechanical properties and subsequently utilised numerical simulations to expand and establish a training dataset.

4.1. Numerical simulation validation

In typical self-centring structures, beams and columns can retain their elasticity even under a significant interstorey drift; however, the masonry infill wall sections may sustain considerable damage. Experimental studies by Guo et al. [31] showed that in self-centring

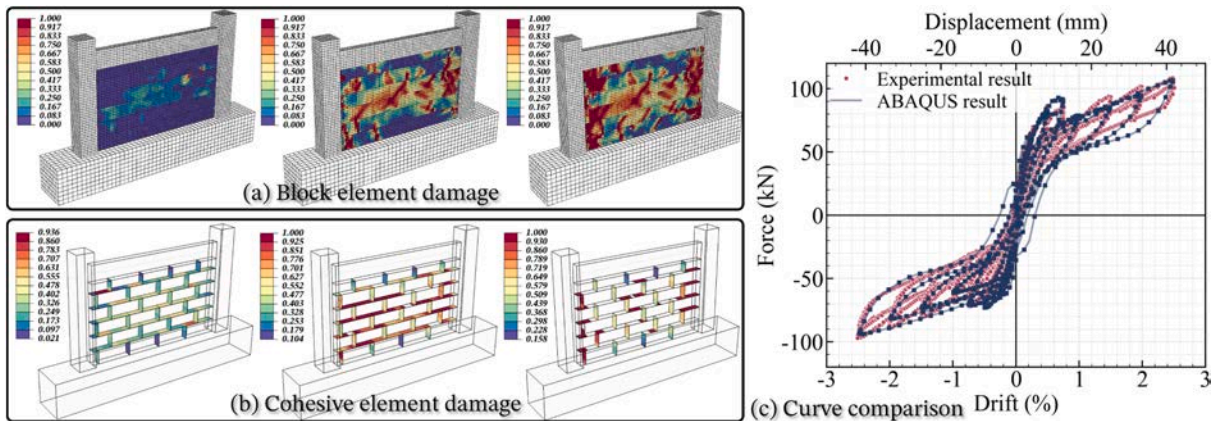


Fig. 4. Microscopic refinement finite element simulation of masonry infill walls.

structures, when the interstory drift reached approximately 0.5 %, large cracks appeared at the corners of the walls. As the displacement increases, additional transverse mortar joint failures occur. A typical hysteresis curve for a self-centring frame structure with a masonry infill wall is shown in Fig. 4. A refined microscopic finite element simulation was conducted based on the experimental results to verify the reliability of the numerical simulation method. For the frame-infilled masonry wall structures, the interaction between the wall and frame significantly affected the simulation results. Therefore, it is essential to consider the internal cracking of the infill wall, particularly under rare seismic events where secondary contact occurs between the blocks after the failure of the mortar joints. Consequently, the use of a separate refined finite element simulation is a more accurate approach for this scenario. In this study, the blocks were simulated using a plastic concrete damage (CDP) material with an elastic modulus of 2600 MPa and a compressive strength of 2.44 MPa [31]. The mortar joints were modelled using cohesive elements [35] with a compressive strength of 3.50 MPa and a shear strength of 0.23 MPa. The contact properties between the blocks were predefined to simulate the compressive and frictional behaviours of the cohesive elements following damage. The simulation results of damage development in the masonry units and mortar layer are illustrated in Fig. 4(a) and (b), respectively. At a structural drift ratio of 0.5 %, cracks appeared and subsequently crushing occurred at the four corners of the masonry infill wall, which was reflected in a sudden drop in the simulated hysteresis curve. When the structural drift ratio reached 1 %, mortar failure led to numerous transverse through-cracks in the infill wall. In the simulation results, cohesive elements also showed significant shear damage, and transverse cohesive elements failed, resulting in through-cracks. These observations were consistent with the experimental results, demonstrating that the micro finite element simulation method employed in this study could accurately capture the seismic damage behavior of masonry infill walls.

Polyakov et al. [42] proposed equivalent infill walls with diagonal compression-only struts to simulate the contribution of walls to the frame, which offers a clear conceptual framework and well-defined loading conditions. In OpenSeesPy, truss elements can be employed to model this behaviour. Nafeh et al. [43] suggested the use of a piecewise linear relationship to define the interstory shear versus displacement for equivalent struts of infill walls. Therefore, in this study, cohesive materials were used to represent the mechanical behaviour of symmetrically arranged diagonal compression struts simulating infill walls. The modelling approach for the frame beam-column joints is shown in Fig. 5. Except for the core region of the joint, the remaining parts were modelled using dispBeamColumn elements. At the contact surfaces of the joints, an elastic-no tension (ENT) material was employed to simulate the opening observed in the joint area of the self-centring structure under large deformations. A comparison of the experimental and macroscopic finite element simulation results is presented in Fig. 5(b). Although there is some discrepancy in the residual deformation at smaller drifts, the shapes of the hysteresis curves and load-bearing capacities satisfactorily agree, providing sufficient accuracy for the macroscopic simulation of the infill walls.

4.2. Dataset development

The prototype structure in this study was derived from the PRESSS design handbook [44] and consists of a five-story self-centring structure located in Wellington, New Zealand. Zhang et al. [45] designed a four-span self-centring frame based on this prototype structure, as shown in Fig. 6(a). The aforementioned macroscopic and microscopic FEM methods can accurately simulate the mechanical properties of infill walls; therefore, both approaches were applied to the walls of the prototype structure. As shown in Fig. 6(b) and (c), a macroscopic finite element model of the overall self-centring structure with masonry infill walls and a microscopic finite element model of a single infill wall were established.

The subject of the prediction in this study was the seismic damage progression of the infill walls, with the damage level determined by the CDP damage factor. The process of extracting the damage factors for the infill walls is illustrated in Fig. 7. First, a macroscopic finite element model of the overall structure was established using OpenSeesPy, followed by incremental dynamic analysis (IDA) to assess the damage probability of the structure. Subsequently, the characteristics of the seismic waves were extracted and clustered to select the representative ground motions and obtain the maximum interstory displacement time history of the structure under extremely rare seismic events, as shown in Fig. 7(b). The infill wall in the middle span was selected to establish the numerical model, with the interstory displacement time history applied as the loading pattern for the microscopic finite element model to evaluate the

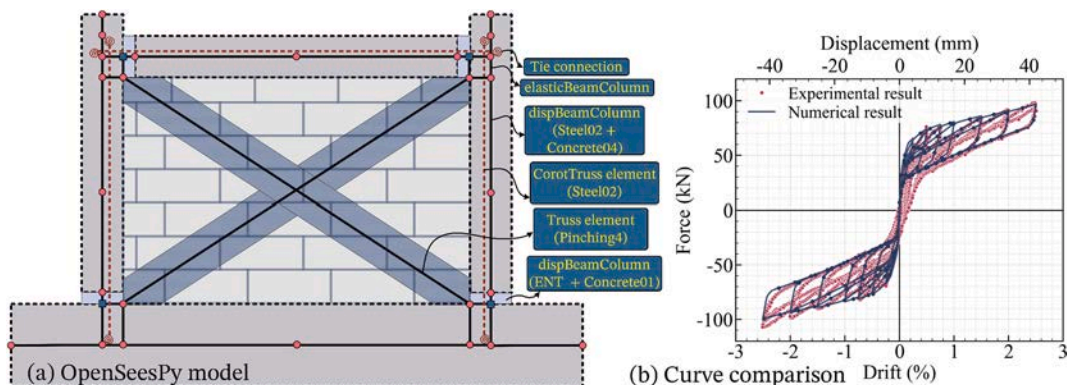


Fig. 5. Macroscopic finite element simulation of masonry infill walls.

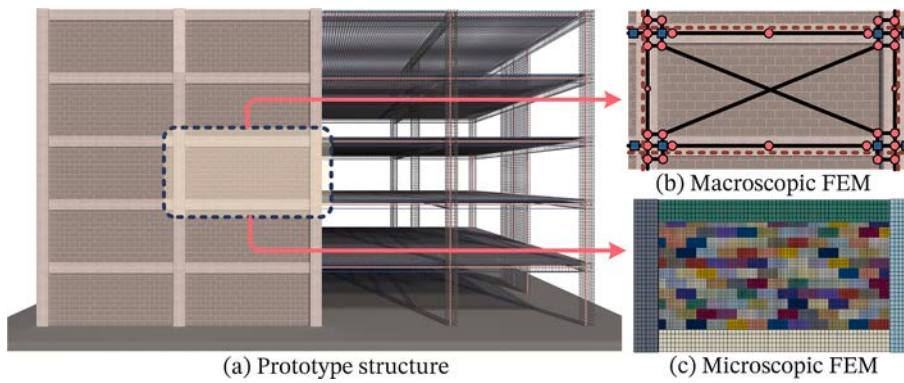


Fig. 6. Prototype structure and FEM methods.

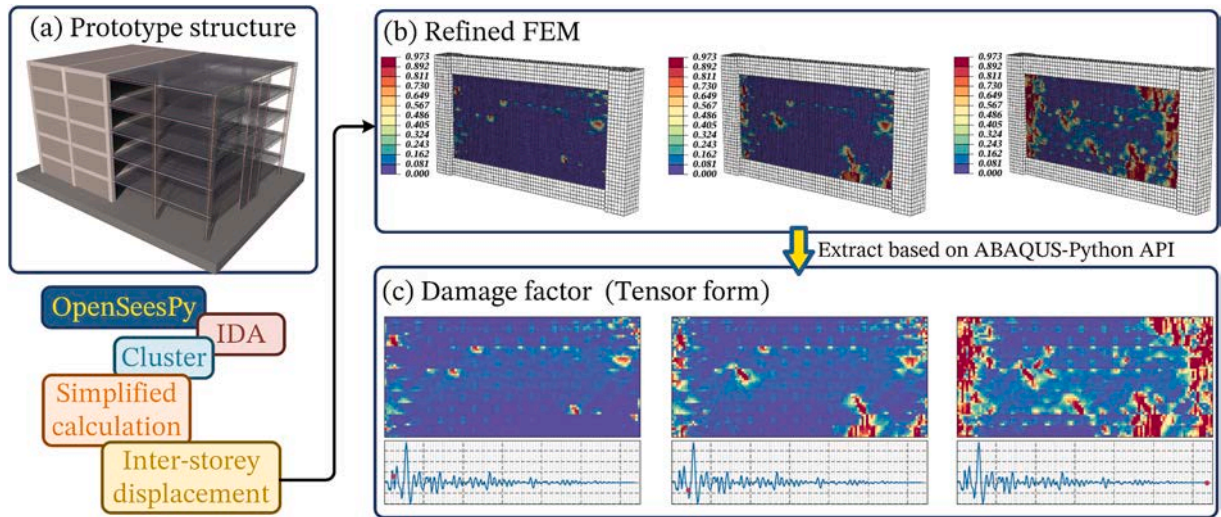


Fig. 7. Extraction process of damage factors for infill walls.

damage to the infill wall during seismic events. Finally, the damage status of each microelement during the seismic process was extracted, with damage values ranging from zero to one. For clarity, these values are represented graphically, where each pixel corresponds to a microelement, as illustrated in Fig. 7(c).

Based on the target response spectrum for Site Class II according to the Chinese seismic design code (GB 50011–2010) [46] for eight-degree frequently occurring earthquakes, 50 natural earthquake ground motions were selected from the PEER database. The first three natural periods of the prototype structure were 0.95, 0.30, and 0.17 s, respectively. The selected ground motions exhibited spectral acceleration during these three periods that followed a normal distribution, and the average acceleration response spectrum

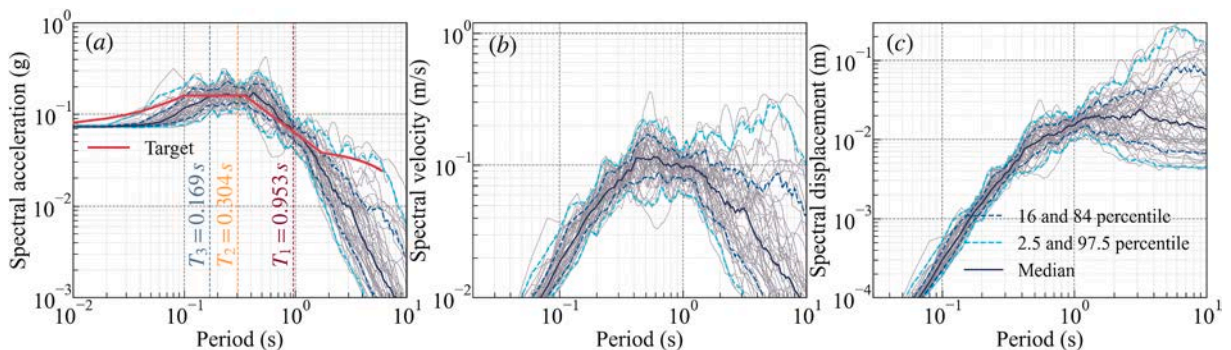


Fig. 8. Response spectra of ground motion records (5% damping ratio): (a) acceleration, (b) velocity, and (c) displacement.

showed an error of less than 5 % compared with the target spectrum, as shown in Fig. 8. Using the 50 selected ground motions, the IDA was performed on a macroscopic finite element prototype structure developed using OpenSeesPy. The peak ground acceleration (PGA) of the ground motions was scaled from 0.01 to 1.0 g, and dynamic time history analyses were conducted. The maximum interstory drift (θ_{max}) versus the PGA curve is presented in Fig. 9(a). Although the computational resources required for extensive time-history analysis in macroscopic FEM are generally acceptable, using the results from 50 seismic events as individual inputs for further calculations in microscopic finite element analysis would result in a significantly low computational efficiency. Feng et al. [47] proposed a seismic clustering method that captured the characteristics of seismic motions and selected a representative subset of seismic events, thereby streamlining numerous seismic motions. As shown in Fig. 9(b), principal component analysis (PCA) was first conducted on the numerous characteristics [47,48] of the seismic motions to reduce the features to two principal components. Subsequently, the bisecting K-means method was employed to cluster the seismic motions, resulting in a reduction from 50 seismic waves to six representative waves. In Fig. 9(c), the dotted line represents the analysis results of 50 seismic motions, whereas the square line corresponds to the analysis results obtained after reducing them to six seismic motions. The clustering results indicate that the analyses for both sets yield similar outcomes regarding the seismic fragility of the prototype structure, particularly when the PGA is below 0.6 g, where the error in the probability of collapse exceeds 2.5 %. This further validates the reliability of the clustering method for reducing seismic motion. Consequently, the subsequent macroscopic FEMs and establishment of the dataset were based on these six seismic motions.

The macroscopic FEM results for the maximum interstory displacement of the six seismic waves under extremely rare earthquakes (EREs) were extracted and used as inputs for the microscopic finite element simulations. Each condition was divided into 1000 analysis steps, resulting in 6000 sets of damage factors, of which 5000 sets were utilised as the training set. Additionally, microscopic simulations of the infill walls under the El Centro seismic motion were conducted, yielding another 1000 sets of damage factors, thereby expanding the test set to 2000 sets.

5. Training methods for the damage inversion model

The damage inversion model (DIM) for infill walls proposed in this study is based on the fundamental principles of the diffusion model and employs a text-to-image approach [49]. This model aims to map the structural deformation and other indicative features of the damage factors of infill walls by representing the damage distribution using a three-dimensional tensor.

5.1. Diffusion model architecture

The DIM mainly consists of three parts: noise generation, conditional mapping, and image generation. During the noise generation process, noise was gradually added to the generated results at each diffusion step. The addition of the Gaussian noise is given by Eq. (3), where β_1 is 0.0001 and β_{1000} is 0.02. Therefore, as the number of diffusion steps increased, the amount of noise added decreased, with the final number of diffusion steps being 1000. The input conditions of the DIM primarily rely on two multilayer perceptrons (MLPs) to map the features. The input features for the DIM consisted of five parameters, all derived from the inter-story displacements of the structure. These features include the maximum positive (D_{max}) and negative (D_{min}) deformations experienced by the infill wall during the displacement time history, current deformation (D), area under the envelope of the displacement–time curve (S), and number of intersection points where the displacement equals zero (N). The two MLP consisted of two hidden layers and ReLU for activation, which was then mapped to a tensor $\in \mathbb{R}^{1 \times 256}$. The dimensions of this tensor were subsequently expanded and ultimately input into each downsampling and upsampling layer of the UNet architecture.

The main body of the DIM is a UNet structure. UNet, a well-known semantic segmentation model, has been widely used for injury identification. As shown in Fig. 10, in the diffusion backbone, UNet is mainly composed of encoder and decoder parts, all of which are downsampling blocks. Unlike the traditional UNet, the UNet proposed in this study uses two types of downsampling blocks. The input of each layer adds the time step and features together and then performs the convolution operations. In the downsampling and

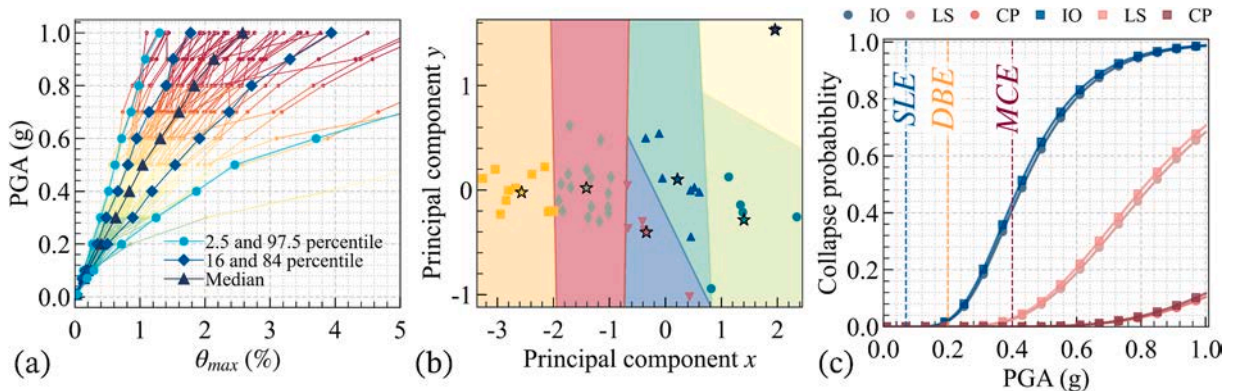


Fig. 9. K-means-based selection of ground motion: (a) IDA curves, (b) clustering results, and (c) comparison of fragility curves.

upsampling blocks, a group normalisation method was adopted, which divided the input channels into groups such that each group had independent statistics. This makes the model training more stable in cases with smaller batch sizes. The activation function used in the UNet system was SiLU. Compared with the ReLU, the SiLU has a smoother curve near zero, and because it uses the sigmoid function, it can maintain an output range between 0 and 1. In addition to the ordinary downsampling and upsampling blocks, the DIM also uses blocks with self-attention. The specific calculation of the attention mechanism can be separated into two processes. The first calculates the weight coefficients based on the query and key, and the second achieves a weighted sum of the values according to the weight coefficients. The first process can be further divided into two stages: the first calculates the similarity or correlation between the query and key, and the second normalizes the original scores of the first stage, as shown in Eq. (13). The final output dimensions of the DIM $\in \mathbb{R}^{1 \times 64 \times 128}$, which was used to predict the damage factor distribution of BIW under the corresponding interstory displacement.

$$\text{Attention}(Q, K, V) = \text{softmax}\left(\frac{QK^T}{\sqrt{d_k}}\right)V \quad (13)$$

5.2. Calculation methods for damage-state prediction error metrics

The error calculation method for the damage factor distribution generated by the DIM and finite element analysis results is illustrated in Fig. 11. This method employs six error calculation techniques: structural similarity (SSIM), root mean squared error (RMSE), mean squared error (MSE), peak signal-to-noise ratio (PSNR), normalised mutual information (NMI), and mean absolute percentage error (MAPE). SSIM is used to measure the structural similarity between the diffusion and FEM results, which is more conducive to evaluating the discrepancies between the observed and predicted outcomes as well as improving the accuracy of the generated damage factor distribution, defined as follows:

$$\text{SSIM}(x, y) = \frac{(2\varphi_x\varphi_y + \omega_1)(2\tau_{xy} + \omega_1)}{(\varphi_x^2 + \varphi_y^2 + \omega_1)(\tau_x^2 + \tau_y^2 + \omega_2)} \quad (14)$$

$$\varphi_x = \frac{1}{N} \sum_{i=1}^N x_i \quad (15)$$

$$\tau_x = \sqrt{\frac{1}{N-1} \sum_{i=1}^N (x_i - \varphi_x)^2} \quad (16)$$

where φ_x and φ_y are the mean values of the observed and predicted values, respectively, τ_x and τ_y are their standard deviations, and τ_{xy} is their covariance. ω_1 and ω_2 are constants, introduced to avoid computational errors when the denominator is zero. The SSIM value ranges between 0 and 1; the closer the SSIM value is to 1, the more similar the finite element analysis results are to the DIM prediction

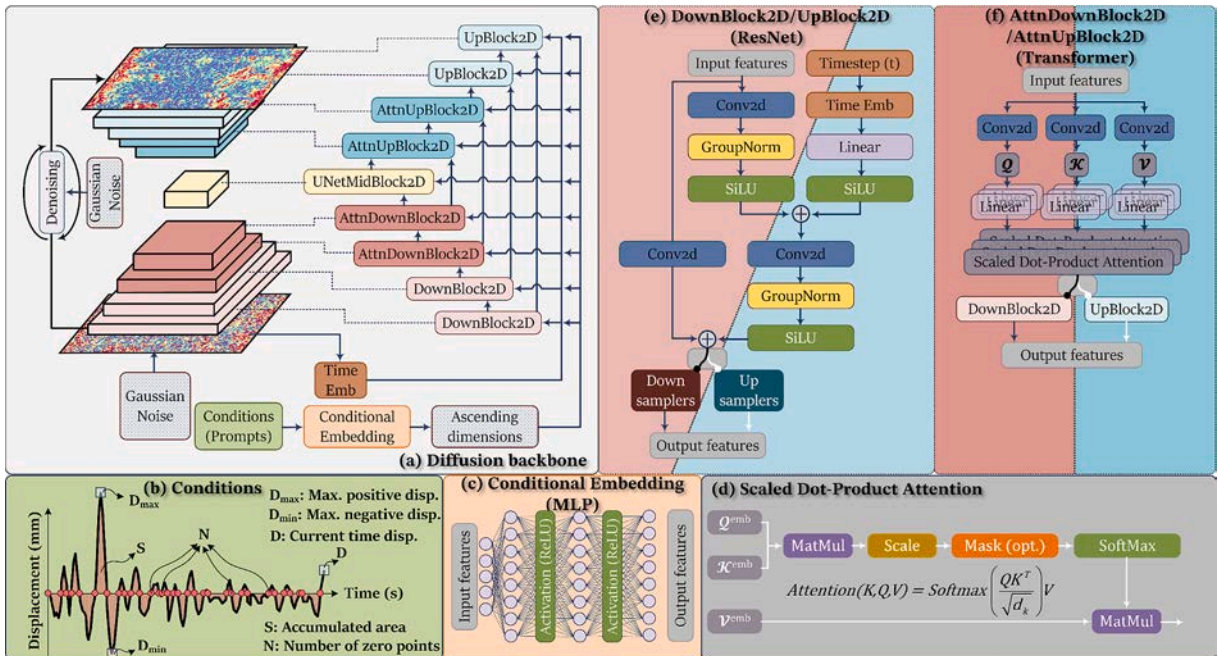


Fig. 10. Architecture of the proposed DIM.

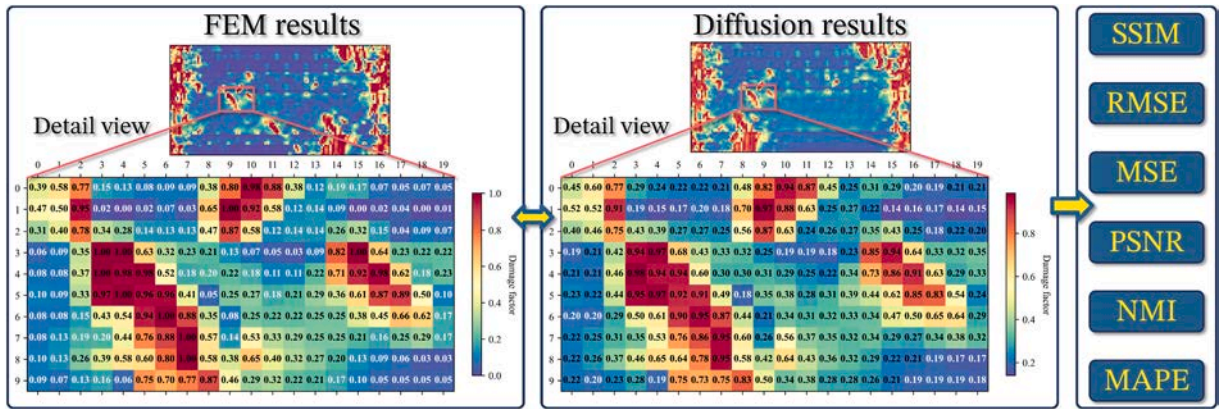


Fig. 11. Error calculation between the FEM and diffusion results.

results. An SSIM value of 0.8 indicates a high degree of similarity between the prediction results and the observation results, while a value above 0.9 suggests that there is almost no noticeable difference between the predicted damage and the actual results.

6. Inversion results for masonry infill wall damage

6.1. Single-step sampling process

The process of generating the DIM for the distribution of the damage factors in the infill walls is illustrated in Fig. 12. Initially, the generation involved pure Gaussian noise. Upon inputting the generation conditions, the DIM can predict this noise while simultaneously removing a portion from the initial noise. This process was repeated to obtain the damage distribution under specified conditions. As illustrated in Fig. 13, if the DIM is not iteratively applied and only single-step sampling is conducted, the resulting damage distribution may be ambiguous or may not yield accurate results. Fig. 13(a) shows six known damage factor distributions to which varying degrees of noise were added, increasing from left to right. In Fig. 13(b), the first damage state has the least amount of noise added, making it the closest to the original results, with an SSIM of 0.43 when compared to the observed values. By contrast, the last damage state had the highest noise level, resulting in an SSIM of 0.008 in relation to the observed damage factor distributions. If the trained DIM is used solely as a denoiser to remove noise from the disturbed damage data distribution, the denoising process, when conducted only once, yields the results shown in Fig. 13(c). After a single denoising process, the SSIM for data with a lower degree of degradation did not show any improvement; for instance, the SSIM of the first damaged state in Fig. 13(c) was 0.25. However, as the degree of data degradation increased, the effectiveness of noise removal through a single-step prediction also improved, with the SSIM of the last damaged state increasing to 0.02, indicating a significant enhancement compared with the pre-denoising results.

6.2. Multi-step sampling process

Although the single-step generation process cannot transform the Gaussian random noise into the desired damage distribution, it exhibits denoising capabilities. Starting with a completely random noise and repeatedly applying this denoising process, the initially vague predicted damage distribution can be progressively refined into a clearer representation. During the training of the DIM, the number of iterative steps for adding noise was set to 1,000. Consequently, the process of generating the damage factor distribution through circular sampling was divided into 1,000 steps. Under different seismic conditions, the damage distribution of the same masonry infill walls varied significantly, as shown in Fig. 14. Although the final damage patterns in all six scenarios indicated severe damage at the contact points between the wall and the columns, the development of damage in the middle of the wall differed substantially in detail. This variation was attributed to the mutual contact and compression of the masonry units following the failure of the mortar joints. Taking Fig. 14(a) as an example, the input at the initial step is the two-dimensional noise generated from a standard Gaussian distribution with a mean of zero and a variance of one. At this stage, the SSIM with respect to the FEM results was only 0.0004, indicating that the damage distribution at the initial step was random and did not correlate with the actual results. Because random noise was introduced into the DIM, five features extracted from the structural deformations corresponding to the

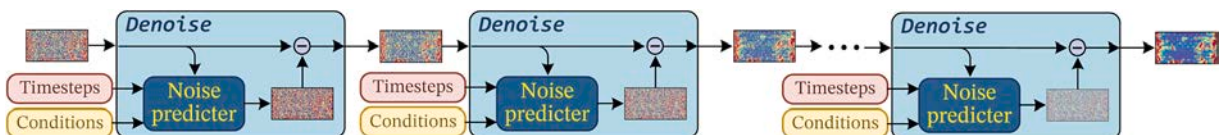


Fig. 12. Generation process of the DIM.

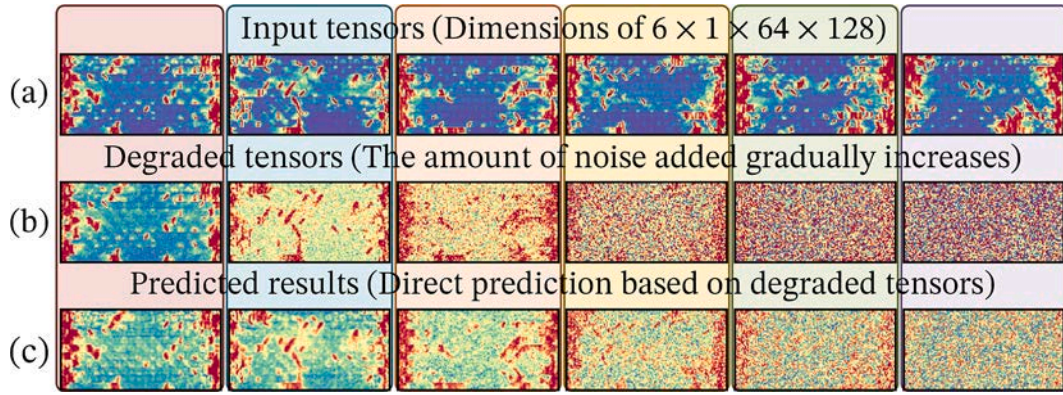


Fig. 13. Single-step generation of the damage factor distribution.

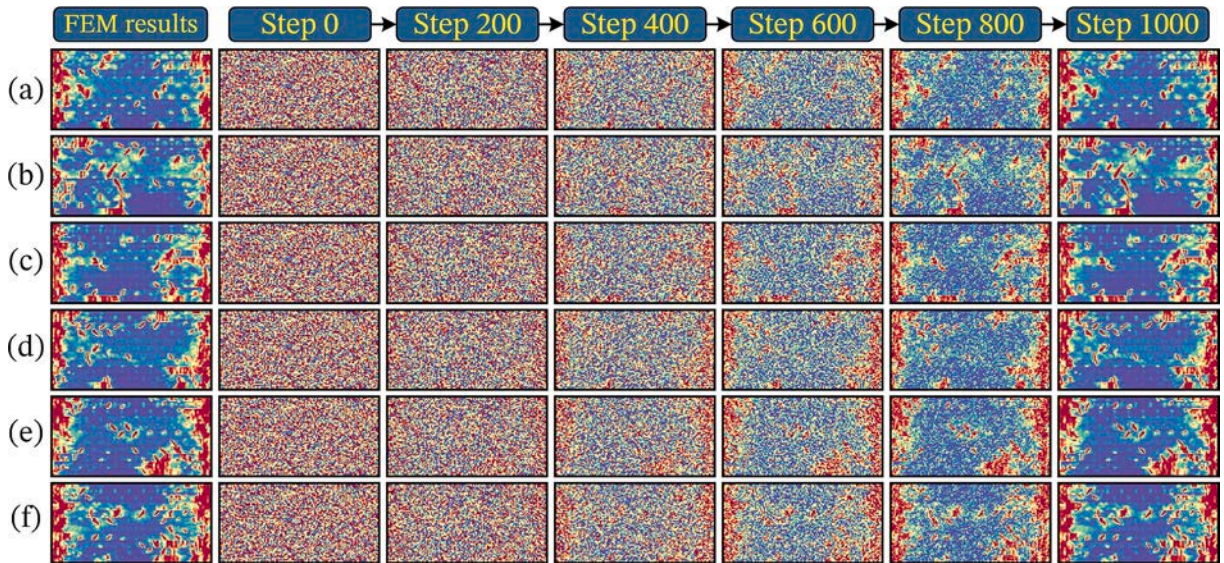


Fig. 14. Multi-step generation of the damage factor distribution.

damage distribution were provided as diffusion-guidance conditions. By the 600th sampling step, the SSIM reaches 0.23. Although this value is not high, it allows for the preliminary identification of the red areas, indicating regions of severe damage that can be predicted. At the 800th step, the SSIM increases to 0.45, and ultimately, the SSIM of the final predicted result exceeds 0.9 when compared with the FEM results, confirming that the DIM can achieve a high-quality damage factor distribution for masonry infill walls after a continuous sampling process of up to 1,000 steps. The scenarios depicted in Fig. 14(b) to (f) are fundamentally similar to the aforementioned case. Compared with the single-step direct-prediction results, the multi-step predictions enable the transformation of abstract damage occurrence conditions into damage-factor distributions for masonry infill walls.

Similarly, multi-step predictions can be made for the damage evolution process of the entire masonry infill wall during an earthquake, as shown in Fig. 15. Eight damage states were randomly selected in sequence from the displacement–time history, as shown in Fig. 15(a)–(h). Initially, the infill wall exhibited no damage with a damage factor of 0. Subsequently, the damage gradually increases and is primarily concentrated at the mortar joint connections of the masonry. At this stage, although the damage factor was dispersed, the overall damage remained relatively minor, as illustrated in Fig. 15(b) and (c). When the sampling step was set to 140, the predicted damage distribution was not sufficiently accurate for small interstory displacements. This was attributed to the fact that many regions had a damage factor that was strictly zero, whereas the predicted results often yielded small nonzero values, resulting in a relatively high error rate. This prediction error can be further mitigated by increasing the number of sampling steps. However, for the distribution of masonry infill wall damage, the inaccuracy in predicting the damage state under small displacements does not affect the overall prediction of the wall damage development process. This phenomenon is illustrated in Fig. 15(a)–(c). As the displacement increases, the accuracy of the DIM predictions improves. At the maximum deformation, the SSIM between the DIM and FEM results was 0.79, as shown in Fig. 15(g). These findings indicate that the DIM can predict the development of damage distribution in masonry infill walls under time-series conditions.

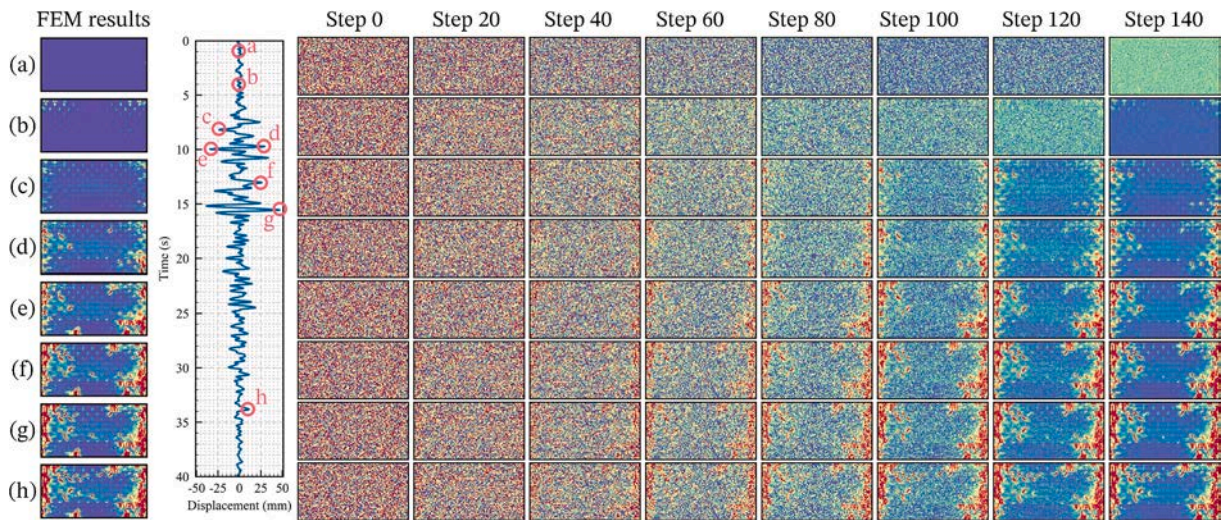


Fig. 15. Generation of the development process of damage factor distributions.

6.3. Different sampling methods and steps

As a critical component in the generation of damage distribution for infill walls using the DIM, the variation in sampling steps significantly impacts the inversion results, as illustrated in Fig. 16. When the sampling step was set to 100, the prediction of the damage location was inaccurate, demonstrating an SSIM of 0.53. As the number of sampling steps increased to 200 and 300, the prediction of the main damage locations became more accurate. However, specific damage areas remained undetected, leading to an SSIM increase of 0.66. When the sampling step reached 500, the predicted results aligned closely with those obtained from the FEM, yielding an SSIM of 0.87, indicating an accurate inversion of both the damage distribution and specific damage values.

At each step of generating the damage distribution, the DIM takes an input that incorporates a certain amount of noise and predicts the noise to estimate the damage distribution under noise-free conditions. When the number of steps is limited, the prediction results are suboptimal; therefore, it is necessary to decompose the prediction process. As illustrated in Fig. 17, this refers to the previously described prediction process, which utilises 600 prediction steps. Predictions were made under five different conditions across four random scenarios, and the results were largely consistent with those obtained using the FEM. However, generating damage distributions using DDPM with hundreds or even thousands of steps require substantial computational resources, which is unfavourable for large-scale damage predictions. Unlike the Markov-based forward process in DDPM, denoising diffusion implicit models (DDIMs) [50] propose a non-Markovian forward process. In contrast to DDPM, sampling in DDIMs is deterministic; that is, given the same initial noise x_t , DDIMs can produce the same result x_0 . Additionally, DDIMs can achieve a more accurate damage distribution with fewer iterations, as illustrated in Fig. 18. The SSIM for the damage distributions generated using the DDPM-based DIM was 0.80, whereas that for the DDIM was 0.68. This discrepancy arises primarily from the differences in the DDIM predictions of the specific damage-factor values. However, the accuracy of the damage-distribution predictions from the DDPM was higher than that of the DDIM. Considering that the sampling steps of DDIM are only 1/20 of those required by DDPM, the accuracy achieved by DDIM is acceptable when considering its computational efficiency.

In addition to the DDPM and DDIM, the noise schedulers diffusion models also include diffusion probabilistic models (DPM++) [51], pseudo numerical methods for diffusion models (PNDM) [49], and the diffusion exponential integrator sampler (DEIS) [53]. The generated damage distributions of the DDPM and DDIM, as well as those of the PNDM and DPM++, under the same sampling steps are compared in Fig. 19. Because of the concentration of damage primarily in the corners of the infill walls under a large interstory drift, the damage factors at the top-left and bottom-right corners of the infill walls were amplified. With only 14 sampling steps, the DDPM is unable to generate an effective damage distribution; however, it can still be observed that the generated results at the 14th step exhibit a damage development trend similar to the FEM results, despite being blurry. In contrast, while the DDIM produces results with an SSIM of only 0.51 under the same sampling steps as the DDPM, there is a noticeable improvement compared to the DDPM. The number of sampling steps for the PNDM and DPM++ was set to seven, which was significantly fewer than that of the other models. The average SSIM of the generated results for these two models was 0.82, indicating that they converged more rapidly, produced higher quality outputs, and achieved faster inference speeds.

An accuracy validation of the damage distribution generated under different noise schedules was conducted on the test set, as listed in Table 1. For the DDPM, the number of sampling steps was set to 1000, resulting in an inference time of 16.12 s per sample on a 2080Ti GPU with 22 GB of memory. However, despite the extensive number of generation steps, it exhibited the highest accuracy, with a MAPE of only 0.04. The generated results indicated that the damage distribution locations were not only more accurate, but the specific damage factor values also aligned more closely with the FEM results. It is noteworthy that the generation results of DEIS demonstrate a significant efficiency advantage; at an RMSE of only 0.03 and a sampling step count of only 10, the generation time per

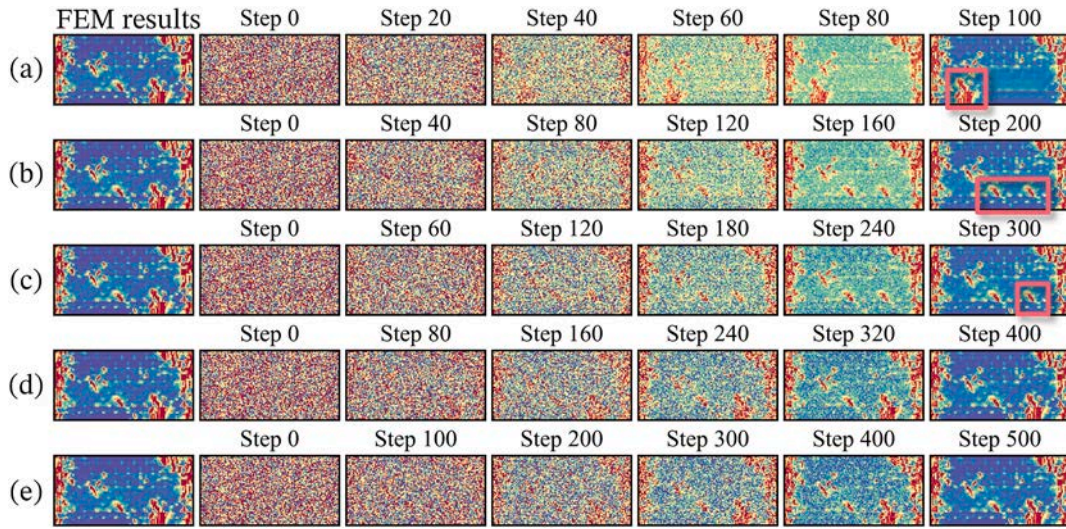


Fig. 16. Distribution of damage factors generated with different sampling steps.

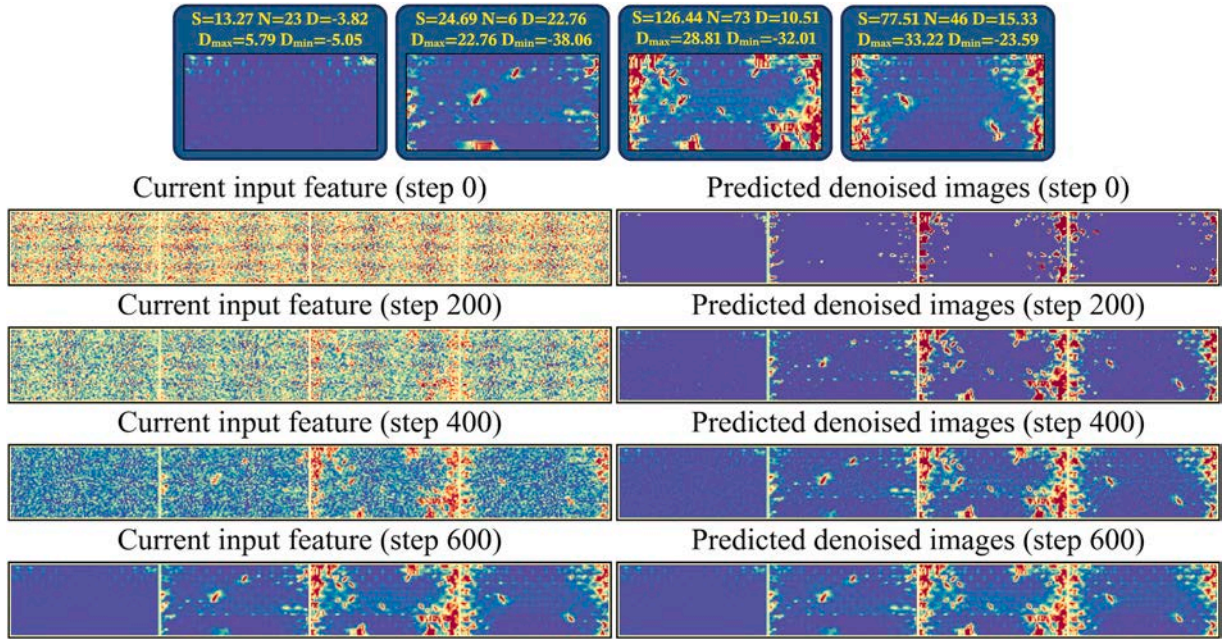


Fig. 17. Sampling process of the DDPM.

sample was merely 0.42 s. This capability enables the rapid and continuous prediction of large-scale damage distributions in masonry infill walls.

7. Discussion

While this study aimed to develop a damage-inversion model that complements traditional FEMs, it has several limitations. In terms of data acquisition methods, the damage distribution of masonry infill walls relies only on microscopic finite element simulations, which involve hundreds or even thousands of contact surfaces for a single infill wall, resulting in extremely low computational speeds. Notably, using a 24-core i9-14900 KF CPU, each condition of a single infill wall in this study required a computation time of more than 48 h, indicating insufficient computational power and an inadequately rich dataset. Moreover, the prompts extracted from the interstory deformations in this study were based on empirical methods. Currently, advanced methods for extracting structural deformation features can be based on VAE. The encoder compresses the interstory deformation information and transforms it into

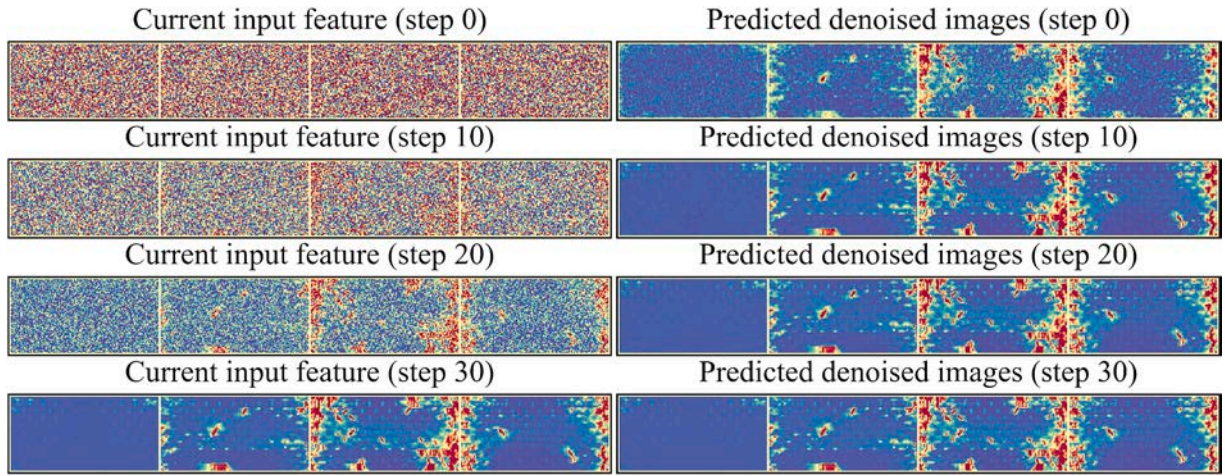


Fig. 18. Sampling process of the DDIM.

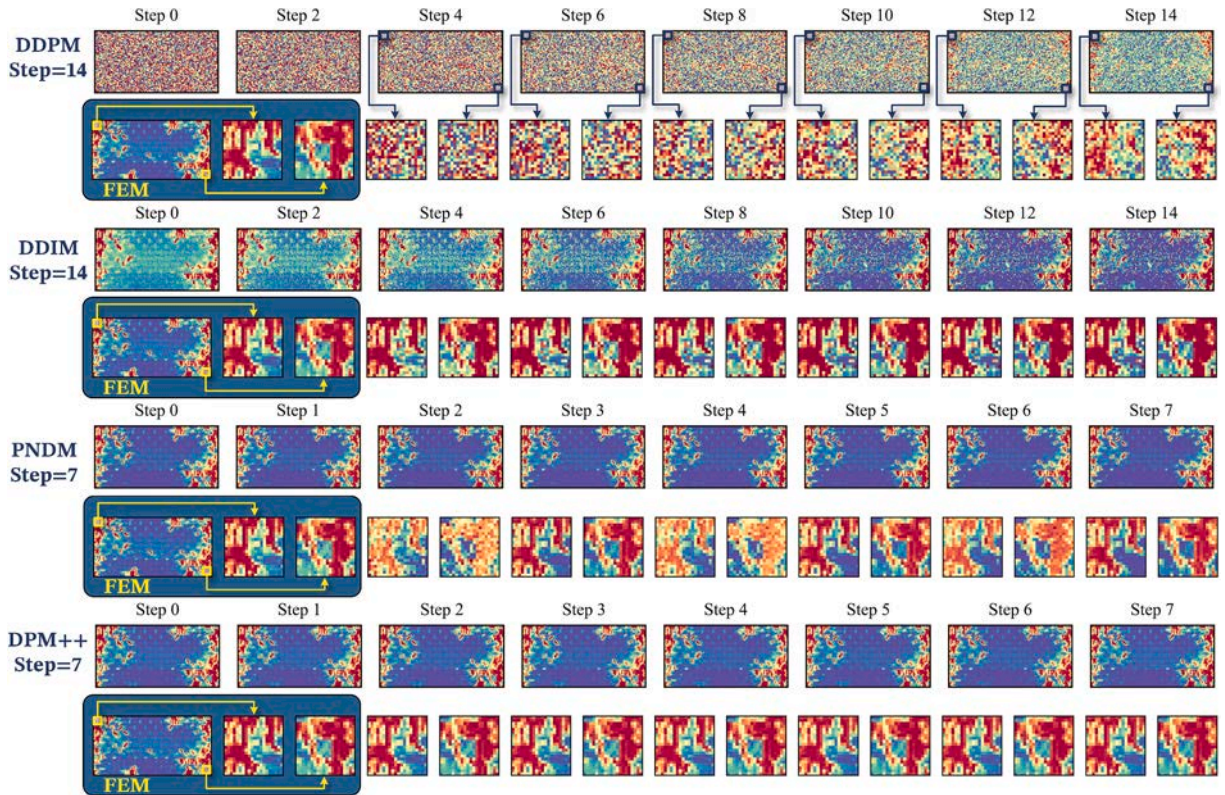


Fig. 19. Sampling process of different noise scheduling methods.

latent space variables. Through VAE, each feature can be represented as a probability distribution, which is then reconstructed using the decoder from the latent variables. The advantage of the VAE-based method lies in its completely unsupervised feature extraction approach. Additionally, the inference network in VAE is used for variational inference on the original input data, generating a variational probability distribution of latent variables. The generative network then reconstructs the approximate probability distribution of the original data from this variational probability distribution of latent variables. This approach significantly reduces the volume of complex displacement signal data, while ensuring that the features can be reconstructed and closely approximate the input signals, thereby minimizing errors introduced by manual feature extraction.

Table 1

Accuracy comparison among different noise scheduling methods.

	SSIM	MSE	RMSE	PSNR	NMI	MAPE	Steps	Per inference time (s)
DDPM[39]	0.95	7.82×10^{-6}	0.002796	52.42	1.79	0.0436	1000	16.12
DDIM[50]	0.89	1.30×10^{-2}	0.114018	41.19	1.66	0.104	100	3.10
LMSE[54]	0.85	1.60×10^{-2}	0.126491	30.01	1.58	0.205	100	1.67
DPM++[51]	0.83	1.50×10^{-2}	0.122474	26.23	1.32	0.149	10	0.15
PNDM[52]	0.82	1.60×10^{-2}	0.126491	23.91	1.31	0.157	10	0.57
DEIS[53]	0.86	1.00×10^{-3}	0.031623	28.88	1.32	0.112	10	0.42

8. Conclusion

This study innovatively proposed an earthquake damage inversion method for infill walls, leveraging diffusion models and using the interstory deformation of the structure at the macroscopic level as prompts to predict the damage distribution of masonry infill walls. This approach provides a novel solution to the limitations of traditional macroscopic FEMs, which cannot capture specific damage evolution patterns, while also overcoming the low computational efficiency of microscopic FEMs. The main conclusions of this study are as follows.

1. Both macroscopic and microscopic FEMs can accurately compute the mechanical behaviour of masonry infill walls; however, they each have significant drawbacks. Neither method can simultaneously achieve high computational efficiency and accuracy, which is detrimental to large-scale structural computations.
2. Prior to performing the microscopic finite element simulations, a fragility analysis based on the macroscopic FEM was conducted. Representative seismic wave conditions were selected by clustering the characteristics of the seismic waves and IDA results. The results indicated that the structural fragility calculations using a reduced set of six ground motions were comparable to those using 50 ground motions, thereby simplifying the computational scenarios for the microscopic model.
3. The DIM, developed based on the diffusion model, can accurately predict the seismic damage distribution of masonry infill walls. The DDPM exhibits high sensitivity to the number of sampling steps, with an SSIM of 0.87 between the DIM predictions and the microscopic finite element simulation results when the number of sampling steps exceeded 500. Therefore, if the DDPM is used for noise scheduling, the number of sampling steps should be greater than 500.
4. Although DDPM achieved the highest prediction accuracy among various diffusion models, DEIS struck a balance between computational efficiency and accuracy. DEIS required only 1/100 of the sampling steps needed by DDPM, achieving an SSIM of 90.51 %. In terms of inference time, DEIS was 7.38 times faster than DDIM. DEIS had the potential to develop an inversion model for the damage evolution process of masonry infill walls based on the full-time history of seismic events.

CRedit authorship contribution statement

Tianyang Zhang: Writing – review & editing, Writing – original draft, Validation, Software, Methodology, Investigation, Data curation. **Yujie Lu:** Writing – review & editing, Software. **Yijie Cai:** Writing – review & editing. **Weizhi Xu:** Writing – review & editing, Supervision, Funding acquisition. **Shuguang Wang:** Supervision, Resources. **Dongsheng Du:** Writing – review & editing, Supervision. **Qisong Miao:** Writing – review & editing, Supervision.

Declaration of competing interest

The authors declare that they have no known competing financial interests or personal relationships that could have appeared to influence the work reported in this paper.

Acknowledgments

The authors are grateful for financial support from The National Natural Science Foundation of China (52208173) and The Natural Science Foundation of the Jiangsu Higher Education Institutions of China (22KJA560003).

Data availability

Data will be made available on request.

References

- [1] W. Bai, J. Dai, R. Liu, Z. Shao, Y. Yang, T. Jiang, B. Zhou, Site investigation on seismic performance of 7 isolated buildings during the 2022 Luding Ms 6.8 earthquake, *J. Build. Eng.* 89 (2024) 109224.
- [2] A. Ihsan Turan, A. Celik, A. Kumbasaroglu, H. Yalciner, Assessment of reinforced concrete building damages following the Kahramanmaraş earthquakes in Malatya, Turkey (February 6, 2023), *Eng. Sci. Technol.* 54 (2024) 101718.

- [3] O. İnce, Structural damage assessment of reinforced concrete buildings in Adıyaman after Kahramanmaraş (Türkiye) Earthquakes on 6 February 2023, *Eng. Fail. Anal.* 156 (2024) 107799.
- [4] M.L. Ivanov, W.-K. Chow, Structural damage observed in reinforced concrete buildings in Adıyaman during the 2023 Türkiye Kahramanmaraş Earthquakes, *Structures* 58 (2023) 105578.
- [5] K. Sharma, L. Deng, C.C. Noguez, Field investigation on the performance of building structures during the April 25, 2015, Gorkha earthquake in Nepal, *Eng. Struct.* 121 (2016) (2015) 61–74.
- [6] B. Zhao, F. Taucer, T. Rossetto, Field investigation on the performance of building structures during the 12 May 2008 Wenchuan earthquake in China, *Eng. Struct.* 31 (2009) (2008) 1707–1723.
- [7] L. Abrahamczyk, D. Penava, S. Markušić, D. Stank, P. Hasan, M. Haweyou, J. Schwarz, Die Magnitude 6,4 – Erdbeben in Albanien und Kroatien – Ingenieuranalyse der Erdbebenschäden und Erfahrungswerte für die Baunormung, *Bautechnik* 99 (2022) 18–30.
- [8] J. Che, Z. Guo, P. Yang, H. Liu, Experimental investigation on seismic behavior of brick masonry wall strengthened with ECC splint, *Constr. Build. Mater.* 391 (2023) 131627.
- [9] L. Jing, N. Wang, S. Yin, Shear performance of textile-reinforced concrete (TRC)-strengthened brick masonry walls, *Constr. Build. Mater.* 397 (2023) 132401.
- [10] J.H. Lee, D.-Y. Yoo, Enhancement of in-plane shear performance in masonry walls strengthened with high-performance fiber-reinforced cementitious composites, *Constr. Build. Mater.* 409 (2023) 133885.
- [11] W.-Y. Lim, Experimental investigation of size effect on unreinforced concrete brick masonry walls under in-plane shear loading, *Constr. Build. Mater.* 428 (2024) 136346.
- [12] W.-Y. Lim, Failure mode dependent shear strength of unreinforced concrete brick masonry wall panels, *Constr. Build. Mater.* 414 (2024) 134976.
- [13] M. Scamardo, S. Cattaneo, P. Crespi, N. Vafa, Cyclic behavior of C-shaped masonry wall retrofitted with twisted bars or bonded rebars, *Constr. Build. Mater.* 443 (2024) 137703.
- [14] M. Vailati, M. Mercuri, A. Gregori, Out-of-plane non-intrusive seismic retrofitting of in-plane damaged masonry infill through 3D printed recycled plastic devices, *Constr. Build. Mater.* 438 (2024) 137256.
- [15] B. Wang, S. Yin, F. Qu, F. Wang, Cyclic shear test and finite element analysis of TRC-reinforced damaged confined masonry walls, *Constr. Build. Mater.* 421 (2024) 135766.
- [16] P. Yang, W. Tian, L. Qing, In-plane shear behavior of brick masonry walls strengthened with basalt textile-reinforced concrete, *Constr. Build. Mater.* 401 (2023) 132732.
- [17] M.S. Ghobadi, R.A. Jazany, H. Farshchi, In situ repair technique of infill masonry walls in steel frames damaged after an earthquake, *Eng. Struct.* 178 (2019) 665–679.
- [18] Z. Chen, Y. Zhou, G. Zhong, Investigation on the influence of previous in-plane loading on the out-of-plane behavior of the innovative damped masonry infill wall, *Eng. Struct.* 308 (2024) 118029.
- [19] Y. Zhou, Z. Chen, G. Zhong, Investigation on the seismic performance of the masonry infill wall with damping layer joint, *Eng. Struct.* 285 (2023) 115979.
- [20] X. Song, Y. Lu, B. Zhang, X. Chen, Seismic behavior of damaged Li-Tie style timber frames with brick masonry infills: Experimental test, finite element analyses, and behavior degradation, *J. Build. Eng.* 86 (2024) 108848.
- [21] M. Agante, A. Furtado, H. Rodrigues, A. Arêde, P. Fernandes, H. Varum, Experimental characterization of the out-of-plane behaviour of masonry infill walls made of lightweight concrete blocks, *Eng. Struct.* 244 (2021) 112755.
- [22] Z.M. Bhat, Y. Singh, P. Agarwal, Cyclic testing and diagonal strut modelling of different types of masonry infills in reinforced concrete frames designed for modern codes, *Eng. Struct.* 317 (2024) 118695.
- [23] N. Maymandi, Y. Liu, G.A. Fenton, Calibration of resistance factors for seismic design of masonry infilled frames using the random finite element method, *Eng. Struct.* 316 (2024) 118590.
- [24] P. Triller, K. Kwiecień, A. Kwiecień, U. Bohinc, B. Zając, M. Tekieli, M. Szumera, T. Rousakis, V. Vanian, A.T. Akyildiz, A. Viskovic, Efficiency of FRPU strengthening of a damaged masonry infill wall under in-plane cyclic shear loading and elevated temperatures, *Eng. Struct.* 317 (2024) 118652.
- [25] X. Xie, Z. Qu, H. Fu, L. Zhang, Effect of prior in-plane damage on the out-of-plane behavior of masonry infill walls, *Eng. Struct.* 226 (2021) 111380.
- [26] D. Penava, V. Sarhosis, I. Kožar, I. Guljaš, Contribution of RC columns and masonry wall to the shear resistance of masonry infilled RC frames containing different in size window and door openings, *Eng. Struct.* 172 (2018) 105–130.
- [27] F. Anić, D. Penava, L. Abrahamczyk, S. Lars, I. Guljaš, On the mechanical behaviour of masonry infilled RC frames, with and without openings, subjected to simultaneous in-plane (IP) and out-of-plane (OoP) loading, *B. Earthq. Eng.* 22 (2024) 1775–1799.
- [28] M. Gorji Azandariani, A. Mohebbkhan, A multi-strut model for the hysteresis behavior and strength assessment of masonry-infilled steel frames with openings under in-plane lateral loading, *Eng. Struct.* 302 (2024) 117433.
- [29] R. Chalabi, O. Yazdanpanah, K.M. Dolatshahi, Nonmodel rapid seismic assessment of eccentrically braced frames incorporating masonry infills using machine learning techniques, *J. Build. Eng.* 79 (2023) 107784.
- [30] Z. Chen, Y. Zhou, W. Lie, X. Fang, Macro-modelling method for the in-plane behaviour of the damped masonry infill wall in a frame structure, *J. Build. Eng.* 80 (2023) 108114.
- [31] R. Zhu, T. Guo, L. Xie, L. Song, K. Yang, S. Tesfamariam, Seismic risk assessment of self-centering prestressed concrete frames with sliding and masonry infill walls: experimental and numerical models, *B. Earthq. Eng.* 22 (2024) 4115–4141.
- [32] X.-L. Gu, T. Zhou, K. Nagai, H. Zhang, Q.-Q. Yu, Prediction of seismic performance of a masonry-infilled RC frame based on DEM and ANNs, *Eng. Struct.* 316 (2024) 118531.
- [33] M. Marinković, C. Butenweg, Numerical analysis of the in-plane behaviour of decoupled masonry infilled RC frames, *Eng. Struct.* 272 (2022) 114959.
- [34] H. Mohamed, A. Furtado, H. Rodrigues, Appraisal of masonry infill walls dynamic characteristics: an analytical study, *Eng. Struct.* 297 (2023) 116995.
- [35] W. Xu, T. Zhang, X. Chen, Q. Miao, S. Wang, D. Du, Experimental and numerical investigation on the seismic performance of masonry walls reinforced by PC panels, *J. Build. Eng.* 58 (2022) 105049.
- [36] J.K. Bhaskar, D. Bhunia, L. Koutas, In-plane behaviour of masonry infill walls with openings strengthened using textile reinforced mortar, *Structures* 63 (2024).
- [37] R. Mudragada, P. Bhargava, Effect of masonry infill on the response of reinforced concrete frames subject to in-plane blast loading, *Structures* 57 (2023).
- [38] P. Zeng, W. Gao, J. Yin, P. Xu, S. Lu, Residential floor plans: Multi-conditional automatic generation using diffusion models, *Autom. Constr.* 162 (2024) 105374.
- [39] A. Nichol, P. Dhariwal, Improved denoising diffusion probabilistic models, *arXiv e-Prints* (2021) arXiv:2102.09672.
- [40] S. Mukhopadhyay, M. Gwilliam, V. Agarwal, N. Padmanabhan, A. Swaminathan, S. Hegde, T. Zhou, A. Shrivastava, Diffusion models beat GANs on image classification, *arXiv e-Prints* (2023) arXiv:2307.08702.
- [41] C. Luo, Understanding diffusion models: A unified perspective, *arXiv e-Prints* (2022) arXiv:2208.11970.
- [42] S. Polyakov, On the interaction between masonry filler walls and enclosing frame when loaded in the plane of the wall, *Transl. Earthq. Eng.* 2 (1960) 36–42.
- [43] A.M.B. Nafeh, G.J. O'Reilly, R. Monteiro, Simplified seismic assessment of infilled RC frame structures, *B. Earthq. Eng.* 18 (2019) 1579–1611.
- [44] S. Pampanin, D. Marriott, A. Palermo, PRESSS design handbook, New Zealand Concrete Society Industry, Auckland, 2010.
- [45] T. Zhang, W. Xu, S. Wang, D. Du, Q. Miao, Study on the evolution of dynamic characteristics and seismic damage of a self-centering concrete structure based on data-driven methods, *Eng. Struct.* 316 (2024) 118529.
- [46] GB50011-2010. Code for seismic design of buildings. China Architecture & Building Press; 2010, Chinese.
- [47] J.-Y. Ding, D.-C. Feng, E. Brunesi, F. Parisi, G. Wu, Efficient seismic fragility analysis method utilizing ground motion clustering and probabilistic machine learning, *Eng. Struct.* 294 (2023) 116739.
- [48] T. Zhang, W. Xu, S. Wang, D. Du, J. Tang, Seismic response prediction of a damped structure based on data-driven machine learning methods, *Eng. Struct.* 301 (2024) 117264.
- [49] J. Ho, T. Salimans, Classifier-free diffusion guidance, *arXiv e-Prints* (2022) arXiv:2207.12598.
- [50] J. Song, C. Meng, S. Ermon, Denoising diffusion implicit models, *arXiv e-Prints* (2022) arXiv:2010.02502.

- [51] C. Lu, Y. Zhou, F. Bao, J. Chen, C. Li, J. Zhu, DPM-Solver++: fast solver for guided sampling of diffusion probabilistic models, arXiv e-Prints (2023) arXiv:2211.01095.
- [52] L. Liu, Y. Ren, Z. Lin, Z. Zhao, Pseudo numerical methods for diffusion models on manifolds, arXiv e-Prints (2022) arXiv:2202.09778.
- [53] Q. Zhang, Y. Chen, Fast sampling of diffusion models with exponential integrator, arXiv e-Prints (2023) arXiv:2204.13902.
- [54] T. Karras, M. Aittala, T. Aila, S. Laine, Elucidating the design space of diffusion-based generative models, arXiv e-Prints (2022) arXiv:2206.00364.